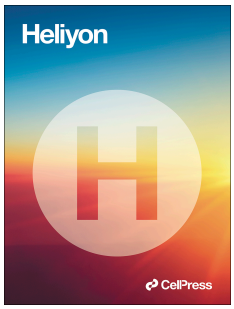

Effect of low temperature calcination on micro structure of hematite nanoparticles synthesized from waste iron source

Juliya Khanam, Md. Rashib Hasan, Bristy Biswas, Md. Farid Ahmed, Sabrina Mostofa, Umme Sarmeen Akhtar, Md. Kamal Hossain, Md.Saiful Quddus, Samina Ahmed, Nahid Sharmin, Sharif Md. Al-Reza

PII: S2405-8440(24)17061-2

DOI: https://doi.org/10.1016/j.heliyon.2024.e41030

Reference: HLY 41030

To appear in: *HELIYON*

Received Date: 5 September 2024

Revised Date: 5 December 2024

Accepted Date: 5 December 2024

Please cite this article as: J. Khanam, M.R. Hasan, B. Biswas, M.F. Ahmed, S. Mostofa, U.S. Akhtar, M.K. Hossain, M.S. Quddus, S. Ahmed, N. Sharmin, S.M. Al-Reza, Effect of low temperature calcination on micro structure of hematite nanoparticles synthesized from waste iron source, *HELIYON*, https://doi.org/10.1016/j.heliyon.2024.e41030.

Effect of low temperature calcination on micro structure of hematite nanoparticles synthesized from waste iron source

Juliya Khanam[a*], Md. Rashib Hasan[b], Bristy Biswas[a], Md. Farid Ahmed[a], Sabrina Mostofa[a], Umme Sarmeen Akhtar[a], Md. Kamal Hossain[c], Md.Saiful Quddus[a], Samina Ahmed[a], Nahid Sharmin[c*], Sharif Md. Al-Reza[b]

[a]*Institute of Glass and Ceramic Research and Testing (IGCRT), Bangladesh Council of Scientific and Industrial Research (BCSIR), Dhaka-1205, Bangladesh*
[b]*Department of Applied chemistry and Chemical Engineering, Islamic University, Kushtia, Bangladesh*
[c]*BCSIR Dhaka Laboratories, Bangladesh Council of Scientific and Industrial Research (BCSIR), Dhaka, 1205, Bangladesh*

Abstract

Hematite (α-Fe_2O_3) nanoparticles have been synthesized from waste source of iron which contains a prominent amount of iron (93.2%) and investigated the effect of low temperature calcination. The two-step synthesis method involved preparing ferrous sulfate through acid leaching process followed by oxidation and calcination at temperatures ranging from 200 to 400°C to produce the desired α-Fe_2O_3 in nano form. The structure, size and morphology of the hematite nanoparticles were characterized using various instrumental techniques including X-ray diffraction (XRD), X-ray photoelectron spectroscopy (XPS), Raman spectroscopy, Fourier transformed infrared (FTIR) spectroscopy, scanning electron microscopy (SEM), transmission electron microscopy (TEM), UV-visible diffuse reflectance spectroscopy (DRS), and a nanoparticle size analyzer. Hematite single phase was confirmed by XRD and the phase occurred at 200°C might indicate the stability range of hematite under certain condition. The average crystal sizes were determined using Debye Scherer formula, modified Scherer formula, size strain plot equation and Halder-Wagner-Langford's method and the results show that crystallite sizes decreased with increasing calcination temperature. XPS analysis confirmed the chemical state (Fe^{3+}) and surface chemistry of the hematite nanoparticles calcined at 300°C. Raman spectrum also supported that the nanoparticles were complete hematite phase and the intensity of all the features decreased with increasing calcination temperature which are consistence with the result obtained from XRD pattern. FTIR spectra of the samples also confirms the XRD results. Morphological analysis obtained from SEM and TEM images suggested the agglomerated irregular spherical nanoparticles with grain size 13.49 nm calcined at 300°C. Band gap energy of the samples were calculated from DRS data and the values ranging from 2.30 to 2.42 eV which are slightly higher than the bulk (~2.1eV). Particles size analysis have been carried out using DLS and Z-average particle size and poly dispersity index (PDI) were measured which indicate the particles are nearly same size (220 to 226 nm).

Keywords: Hematite, Nanoparticle, Recycling, Structure, Morphology, Particle size

*** Corresponding author**: Institute of Glass and Ceramic Research and Testing (IGCRT), Bangladesh Council of Scientific and Industrial Research (BCSIR), Dhaka-1205, Bangladesh
BCSIR Dhaka Laboratories, Bangladesh Council of Scientific and Industrial Research (BCSIR), Dhaka, 1205, Bangladesh
E-mail address: juliyakhanom@gmail.com, nahid_pppdc@yahoo.com

1. INTRODUCTION

Nanostructured materials research has been attracted much interest due to their wide range of important application and unique physico-chemical properties such as optical, electronic, magnetic properties that diverge greatly from their bulk materials as they have smaller grain size, quantum confinement effect, high sensitivity and high surface to volume ratio [1–4]. Metal-oxide based nanoparticles have become a fascinating growing class of materials due to their exceptional stability, crystallinity, conductivity, biocompatibility and nontoxicity which open the doors for these types of materials to be potential candidates in several applications. Among the various metal oxide nanomaterial, iron oxide nanoparticles have attracted great attention due to their promising applications in gas sensors, magnetic resonance imaging, photo-electrochemical cells, solar cell, contrast agents, drug delivery, pigment, catalysis, environmental application and so on [1,5–9].

Iron oxides are particularly important because of their various applications and it exist in many form in nature including hematite (α-Fe_2O_3), maghemite (γ-Fe_2O_3) and magnetite (Fe_3O_4) in which hematite being probably most common phase. Hematite (α-Fe_2O_3) is a metal oxide n-type semiconductor with a band gap of ~2.1eV which has a potential technological application such as catalysis, pigments, gas sensors, field effect transistor, photo electrolysis reactor, water treatment due to its non-toxicity, low processing cost, high resistance to corrosion , tunable biocompatibility and thermodynamic stability, environmental friendly [1,3,17,5,10–16]. Various physical and chemical methods have been adopted for synthesis of hematite nanoparticles such as electron beam evaporation, sputtering technique, mechanical millings, high energy ball milling, co-precipitation, electrochemical, sol-gel method, ultrasonic irradiation, solvothermal method, combustion, solvent evaporation, spray pyrolysis, solvent extraction [18–20], microwave assisted synthesis [21], green synthesis, thermal transformation technique [22], polyol [23], calcination and so on [24,25]. Many researchers have used calcination and thermal decomposition methods for synthesis of hematite nanoparticles [12,26,27]. Xili et al. [27] synthesized hematite nanoparticles by hydrothermal-calcinaton route as calcination temperature ranging from 400 to 700°C with tunable porous structure. J Sharmila Justus et al. [12] synthesized hematite nanoparticles in which the powders samples were subsequently calcined in air for 3h at three different temperatures ranging from 400 to 800°C. Tati Nurhayati et al. [28] have obtained hematite nanoparticles using microwave assisted calcination method within the temperature range of 250 to 350°C with $FeCl_3.6H_2O$ and NaOH as precursors. They found from the XRD result that hematite formation began at 300°C or slightly

lower than 300°C and the degree of crystallinity increases with increasing the calcination temperature. No phase formation occurred at calcination temperature 250°C indicating the amorphous nature of the samples [28]. Here, we report the synthesis of hematite nanoparticles by oxidation-calcination of ferrous sulfate precursors obtained from waste condensed milk container through acid leaching process. Among the various chemical methods, low temperature calcination has several advantages for large scale synthesis of hematite nanoparticles such as easy and cost effective; no requirement for high pressure, energy, time, temperature and toxic chemicals as well as cheap available raw materials source. The starting source of raw material for the synthesis of hematite nanoparticles is waste condensed milk container having 93.2 % iron [8]. There are many source of iron containing material which used as a solid waste like mill scale, sludge, iron dust, iron scrape, condensed milk container, beverage can, refractories and sinter plant, steel industries and so on. Condensed milk container can be used in many tea stall, restaurants and household purposes in Bangladesh. After using the inner material, the remaining containers are just thrown out drastically in the environment. Solid waste dumping in open spaces is a great concern for environmental issues as the environment and how to save it has been an area of prime focus for the entire world community [29]. So, the implementation of appropriate solid waste management should be taken into account in order to find solutions that are economically appealing and environmentally sustainable [30,31]. Recycling of solid waste products as well as household wastes have been converted into developed and advanced products by attentive manipulation of synthetic condition. The continued development of recycling and recovery technologies for solid waste materials are considered as economically and environmentally viable when the maximum utilization of the waste products have done into value added products by appropriate method.

Based on earlier studies, many researchers have reported that hematite typically forms around 300°C. However, the recent findings indicating that hematite can form at 200°C via the Combustion-Calcination method which open up new avenues for research [32]. The research report here in focusing on the synthesizing hematite nanoparticles from waste condensed milk container through a simple acid leaching method with low temperature calcination which is environmentally friendly. This approach not only utilizes waste materials but also potentially reduces energy consumption compared to traditional high-temperature synthesis methods. The other purpose of this research is to create opportunity for the small entrepreneur so that they can develop an industry in Bangladesh to achieve the vision and mission for sustainable development.

The investigation of structural, morphological, surface chemistry and optical property have been carried out using different technique such as XRD, FTIR, RAMAN, SEM, TEM, DLS, DRS and XPS.

2. METHODOLOGY

2.1 Materials and reagents

Locally available waste condensed milk containers were used as a primary source of iron which contain 93.2% iron [8]. Sulphuric acid, H_2SO_4 (Merck, Germany) and Sodium nitrate, $NaNO_3$ (Merck Germany) were used as received without further purification for the synthesis of hematite (α-Fe_2O_3) nanoparticles.

2.2 Synthesis of hematite

Hematite (α-Fe_2O_3) nanoparticles were synthesized from ferrous sulfate by oxidation-calcination method in which waste condensed milk container cans have been used as a source of iron content for the preparation of ferrous sulfate through acid leaching process [8]. The collected cans were first washed properly and then dried and cut into small pieces for the maximum acid leaching followed by crystallization. A mixture of specified amount of dried ferrous sulfate, $FeSO_4$ and sodium nitrate, $NaNO_3$ were taken in porcelain crucible, according to a designed weight ratio of $FeSO_4$:$NaNO_3$=1:0.02 was maintained. Then the mixture was heated slowly in a burner for a certain period of time and again reheated vigorously for 30 minutes. The resultant burned product of $FeSO_4$ was cooled and grinded and finally the mixture was calcined at 200, 300 and 400°C for 4 hours in a muffle furnace. The product obtained from calcination was cooled, grounded and washed several times to reduce the impurities and soluble component. After that, the washed samples were filtered and dried in an oven at 110°C for two hours. To get the small grain size, the obtained hematite was then again grounded properly.

2.3 Characterization techniques

The structural analysis and phase identification of the samples were carried out by X-ray diffraction (XRD) technique using SmartLab SE, Rigaku, Japan with CuKα radiation (λ=1.540898 Å) source, and 2 theta range of 10° to 80°. Fourier Transform Infrared (FTIR) spectra has been recorded in the range of 400-4000cm^{-1} by using NICOLET iS5, Thermofisher. Surface morphology, grain size and the elemental analysis of the hematite nanoparticles were investigated by scanning

electron microscopy (MA15 VP-SEM, Carl Zeiss Evo, UK) and transmission electron microscopy (JEM-2100 Plus, Japan) with energy dispersive spectroscopy (EDS). Raman spectra were collected by a macroRAM, HORIBA Scientific, Japan Raman microscope with 633nm excitation light in the range 70–1000cm^{-1}. UV–Vis diffuse reflectance spectra (DRS) were obtained by UV–Vis spectrometer Perkin-Elmer, Lamda 1050+ USA, equipped with an integrating sphere and the baseline correction was performed using a calibrated reference sample of powdered barium sulfate ($BaSO_4$). The spectra were recorded at room temperature in the wavelength range of 200–800 nm. Surface chemistry and the chemical state of the synthesized nano particles were explored by X-ray photoelectron spectroscopy (XPS), K-alpha, Thermo Scientific, by using a monochromatic source of Al K-alpha (λ=1486.69 eV) X-ray source. The calibration of the binding energy curves were performed using C 1s peak at 284.8 eV.

3. Results and Discussion

3.1 XRD Analysis

The crystal structure and the purity of the synthesized iron oxide nanoparticles calcined at low temperature ranging from 200, 300 and 400°C were investigated by XRD as represented in Fig.1. All the diffraction peaks of the calcined samples were found to be well matched with the standard α-Fe_2O_3 reflections (JCPDS card No. 01-089-0596) representing that the α-Fe_2O_3 nanoparticles are highly crystalline structure. No other diffraction line corresponding to other phases has been observed, indicating high purity of the samples. It has been also showed that there have a significant change in peaks variation due to different calcination temperature. It is clearly noticed that as the calcination temperature increases, the width of the peaks have been broadened indicating the small crystallite size. Crystallite size increases or decreases is depend on according to ordering inside the material (density of the localized states). Structural and textural properties are normally changed with increase of calcination temperature [33]. The crystallinity of the samples is directly related to the crystallite size [34]. For the identification of level of crystallinity, the average crystal size have been determined by various method including classical Debye-Scherer Formula (CS), the least square modified Scherer Formula (MS), Size strain plot (SSP) method, Williamson Hall (WH) method and Halder Wagner Langford's method (HWL). Moreover, the lattice parameters (a, b, and c) have been calculated by the following expression,

where d is the inter planar distance, a and c are the lattice parameters and h, k, l are the Miller indices [35]. The results are shown in Table 1.

$$d_{hkl} = \frac{1}{\sqrt{\frac{4}{3a^2}(h^2 + k^2 + l^2) \pm \frac{l^2}{c^2}}} \quad (1)$$

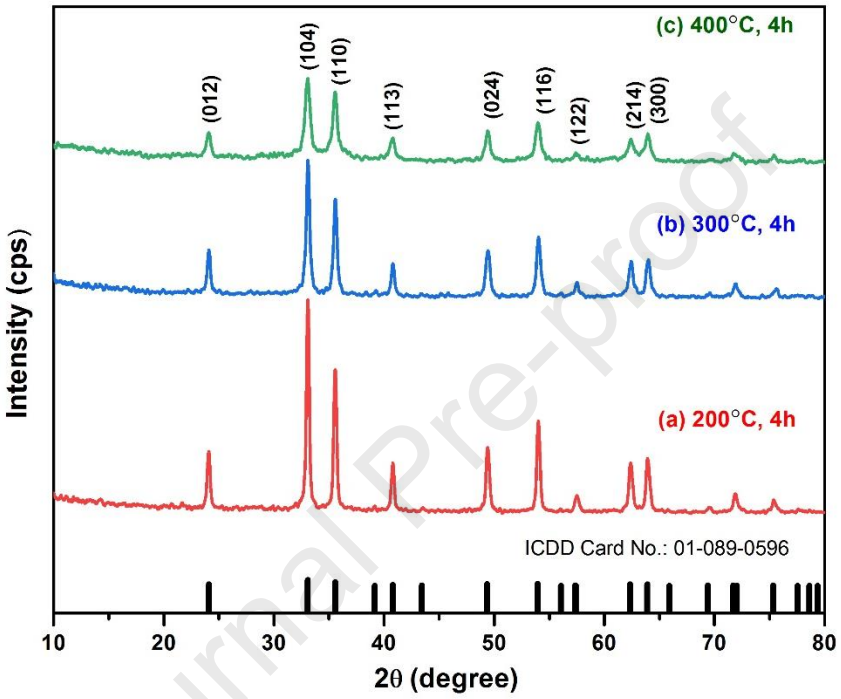

Fig. 1. XRD pattern of α-Fe_2O_3 nanoparticles at different calcination temperatures

3.1 .1 Determination of crystal size

3.1.1.1 Classical Scherer (CS) and modified Scherer Formula (MS)

XRD can be utilized to evaluate peak broadening in the nano crystals with crystallite size and intrinsic lattice strain effects due to dislocation. The peak broadening basically consists of two parts, physical broadening and instrumental broadening which have been measured as full width at half maxima (FWHM). The crystallite size of the α-Fe_2O_3 nanoparticles was measured by the X-ray broadening method using Debye-Scherer Eq. 2 [36,37].

$$D_{CS} = \frac{k\lambda}{\beta \cos\theta} \quad (2)$$

Where *K* refers to the shape factor (0.9), λ is the wavelength of the incident CuKα=1.5406 Å radiation, β is the full width at half maxima (FWHM) and θ is the Bragg diffraction angle. By rearranging Eq. 2 integral breadth can be obtained.

$$\beta = \frac{k\lambda}{D_{CS}\cos\theta} \qquad (3)$$

Modified Scherer equation also obtained by rearranging Eq. 3 and taking logarithm on both side as follows:

$$ln\beta = \ln(k\lambda/D_{M-S}) + \ln(1/cos\theta) \qquad (4)$$

By linear plot of $\ln(1/cos\theta)$ vs. $ln\beta$, the slope and intercept of the fitted line will obtain as modified Scherer equation. Using the obtained intercept, the average crystal size can be calculated by Eq. 4. by following relation:

$$D_{MS} = k\lambda/e^{intercept}$$

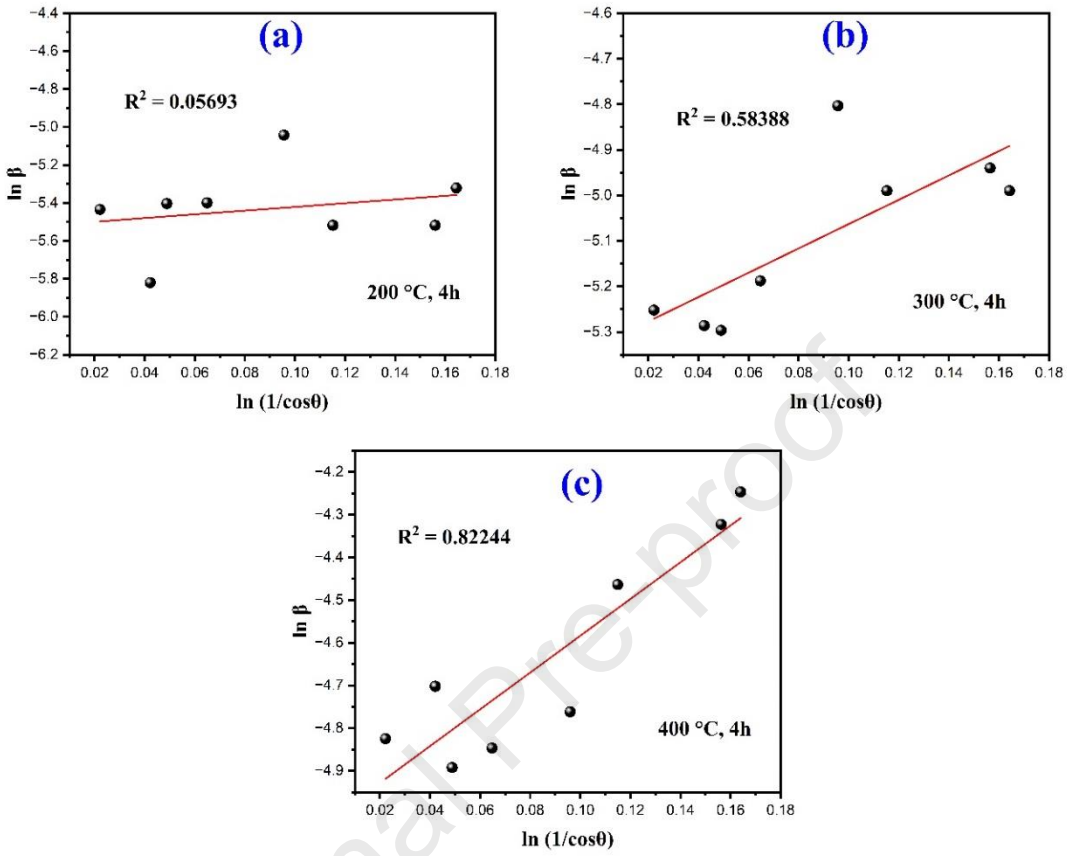

Fig. 2. The least square modified Scherer equation plot of XRD

3.1.1.2 Size-strain plot (SSP)

Size strain plot is one of the peak profile analysis method which considers that XRD peak profile is a combination of Lorentzian function and Gaussian function, where size broadened profile is labeled as Lorentz function and strain broadened profile is labeled as Gaussian function and it expressed as follow [38,39]:

$$(d_{hkl}.\beta_{hkl}.\cos\theta)^2 = k\lambda/D_{SSP}\ (d^2{}_{hkl}.\beta_{hkl}.\cos\theta) + \frac{\varepsilon^2}{4} \quad (5)$$

Where d_{hkl} is the latticle distance between the (hkl) planes. By using the above Eq. (5), a plot is drawn with $(d^2{}_{hkl}.\beta_{hkl}.\cos\theta)$ vs. $(d_{hkl}.\beta_{hkl}.\cos\theta)^2$ corresponding to each diffraction peak, which is shown in Fig. 3. The average crystallite size D, will be obtained from the linear fit slope as given below:

$$D_{SSP} = \frac{k\lambda}{slope} \quad (6)$$

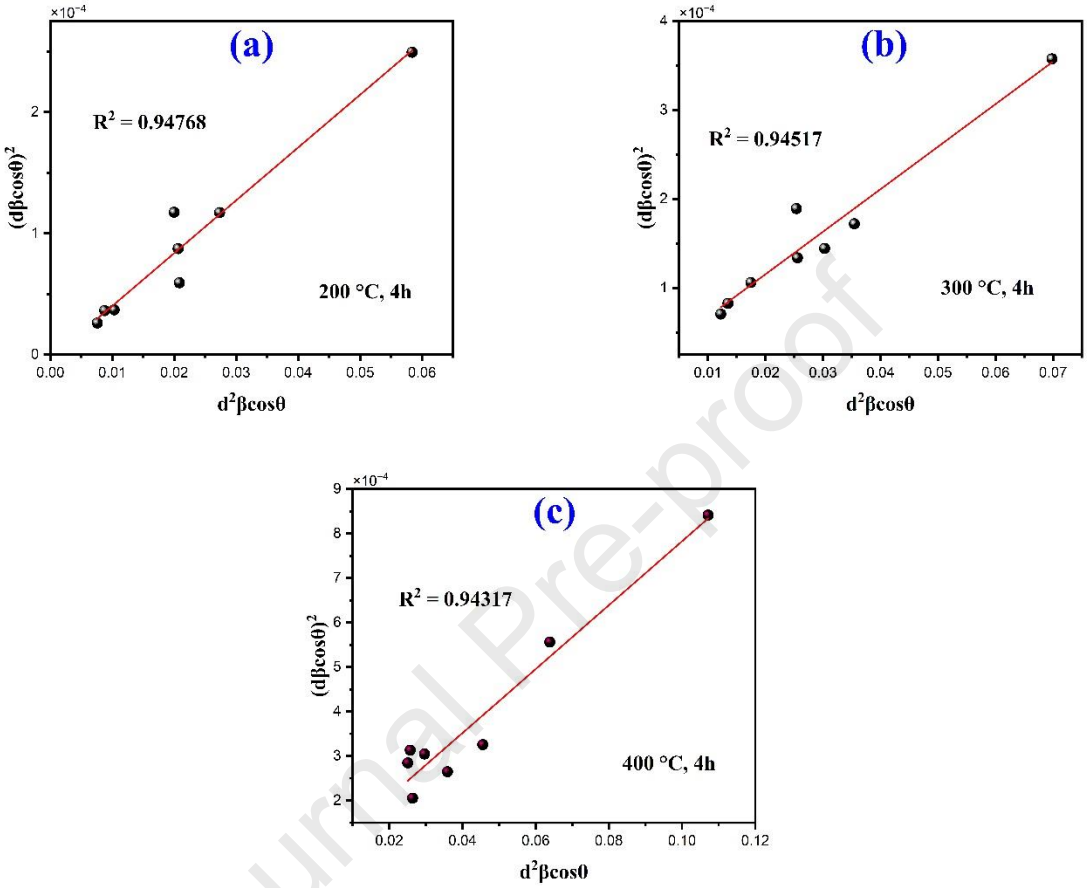

Fig. 3. Size strain plot of the nanoparticles.

3.1.1.3 Halder – Wagner Langford's (HWL) method

The average crystallite size was also determined using the HWL method from the integral breadths, β of the XRD data. In the SSP method the size broadening and the strain broadening of the XRD peak profile have been assumed as a function of Lorentzian and Gaussian function respectively but actually XRD peak is neither Lorentzian function nor Gaussian function. Since the Gaussian function matches the XRD peak region well, but without a match, its tail falls down very rapidly and on the other hand, tails of the profile fits quite well with Lorentz function, but that fails to match the XRD peak region. Therefore, to overcome this Halder-Wagner Langford method is applied in which the peak broadening is a symmetric Voigt function and convolution of

Gaussian and Lorentz functions are used. According to Halder-Wagner method the relation between the crystallite size and the lattice strain is expressed as [40,41]:

$$\left(\frac{\beta^*}{d^*}\right)^2 = \frac{K}{D}\left(\frac{\beta^*}{d^{*2}}\right) + 2\varepsilon^2 \quad (7)$$

Here $\beta^* = \beta cos\theta/\lambda$ and $d^* = 2sin\theta/\lambda$, λ is the X-ray wavelength. By putting the value of β^* and d^* in Eq. (7) and it can be modified as:

$$\left(\frac{\beta cos\theta}{sin\theta}\right)^2 = \frac{k\lambda}{D_{HWL}}\frac{\beta cos\theta}{sin^2\theta} + 16\varepsilon^2 \quad (8)$$

Eq. (8) can also be written as:

$$\left(\frac{\beta}{tan\theta}\right)^2 = \frac{k\lambda}{D_{HWL}}\frac{\beta cos\theta}{sin^2\theta} + 16\varepsilon^2 \quad (9)$$

Now plot the graph $\frac{\beta cos\theta}{sin^2\theta}$ vs. $\left(\frac{\beta}{tan\theta}\right)^2$ along Y-axis for all reflection data, it shows a linear fit with straight line equation where the slope of the line provides the average crystal size D_{HWL} and the intercept gives the strain ε as shown in Fig.4.

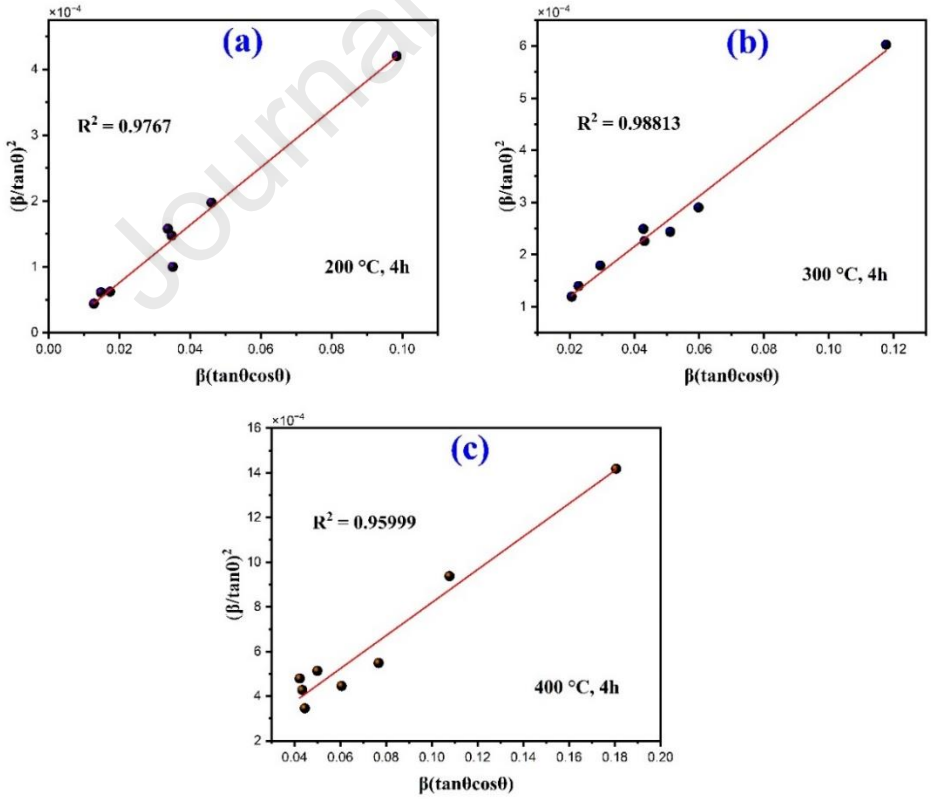

Fig. 4. Halder-Wagner plot of the α-Fe_2O_3 nanoparticles

Table 1

Determination of lattice parameter and crystal size by different method

Sample	Crystal Size (nm)				Lattice parameter	
	D_{CS}	D_{MS}	D_{SSP}	D_{HWL}	a (Å)=b (Å)	c (Å)
200°C, 4h	29.73	34.57	31.87	31.73	5.04235	13.79344
300°C. 4h	21.14	28.63	29.01	28.65	5.03890	13.78402
400°C, 4h	13.07	20.88	19.28	18.76	5.03799	13.78402

The calculated average crystal size determined by different method as shown in Table 1 that the crystallite size decreases as the calcination temperature increases and the calculated values have been changed in different method. Crystallite size ranges vary from 13.07 nm to 29.73 nm for classical Scherrer formula (CS), 20.88 nm to 34.52 nm for modified Scherer formula (MS), 19.28 nm to 31.87 nm for the size strain plot method (SSP) and 18.76 nm to 31.87 nm for Halder Wagner Langfords model (HWL) for calcination temperature of 400, 300 and 200°C. The applied three methods including MS, SSP and HWL give nearly same crystallite size as compared to another method CS in which crystallite size slightly smaller than the other methods. Conversely, the HWL model exhibits the higher degree of accuracy with fitted data as compared to MS method and SSP model and the R^2 values are 0.9767, 0.9881 and 0.9599 for 200, 300 and 400°C respectively.

3.2 SEM and EDS analysis

The characterization of hematite nanoparticles calcined at different temperatures were also carried out using SEM and EDS analysis as depicted in Fig.5. It has been found that the particles are seriously agglomerated and polygonal in shape [42]. Nevertheless, the precise shape and size of the individual nanoparticles could not be decided accurately owing to the formation of large aggregate or cluster [43] as shown in Fig. 5. The image of the synthesis materials revealed an aggregated nature with hematite particles predominating among the various crystal morphologies. EDS spectra also showed the purity of the nanoparticles by getting the three peaks of iron (Fe) and one peak of oxygen (O) for all the synthesized of α-Fe_2O_3 nanoparticles [24].

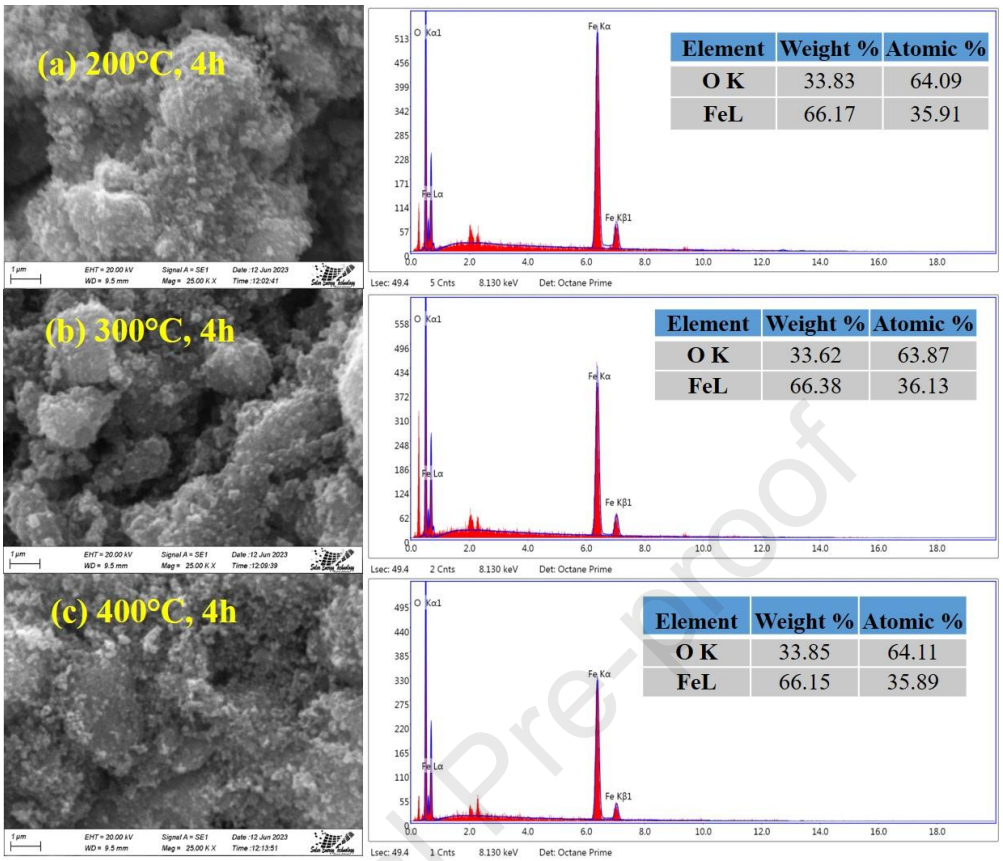

Fig. 5. SEM images (left) and EDS (right) data of α-Fe_2O_3 nanoparticles calcined at different temperature

3.3 FTIR spectroscopic analysis

The functional group and the metal-oxygen bond formation of the hematite nanoparticles has been investigated by Fourier Transform Infrared spectrometer. Fig. 6.represents the absorption data of low temperature calcined hematite nanoparticles which confirmed that the synthesized samples are IR active. The prominent absorption bands observed at 438.65 and 521.51 cm^{-1} are due to metal-oxygen stretching vibration [1,2,42,44,45]. The weak absorption peak observed at 2360 cm^{-1} is an asymmetric stretching peak of CO_2 in the air [46].

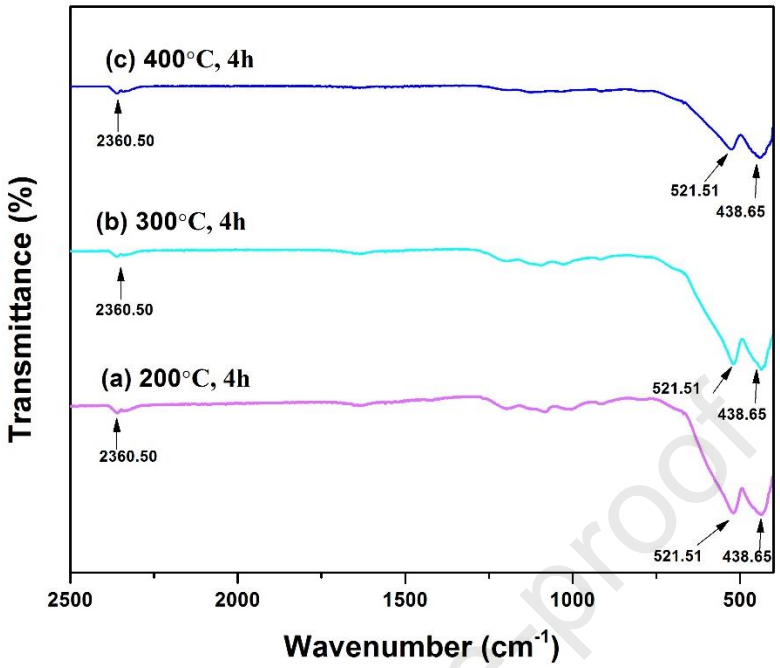

Fig. 6. FTIR spectra of α-Fe_2O_3 nanoparticles at various temperature

3.4 Raman spectroscopic analysis

Raman spectra of the hematite nanoparticles are shown in Fig.7. Seven phonon lines are expected in hematite single crystal structure in which two modes of A1g at about 226 and 496 cm^{-1} and five modes of Eg at about 245, 293, 298, 410, 613 cm^{-1} [35,42,47,48]. The significant four vibration peaks centered at around 226 (A1g), 295 (Eg), 410 (Eg) and 613 (Eg) cm^{-1} are different mode of vibration [49]. A broad band at around 566 cm^{-1} for the sample calcined at 200°C, 4hours is due to the amorphous iron oxides [50]. It was clearly observed from Fig. 7 that the intensity of the all the Raman peaks decreased with increasing calcination temperature which also indicated the lower crystallite size confirmed by XRD analysis.

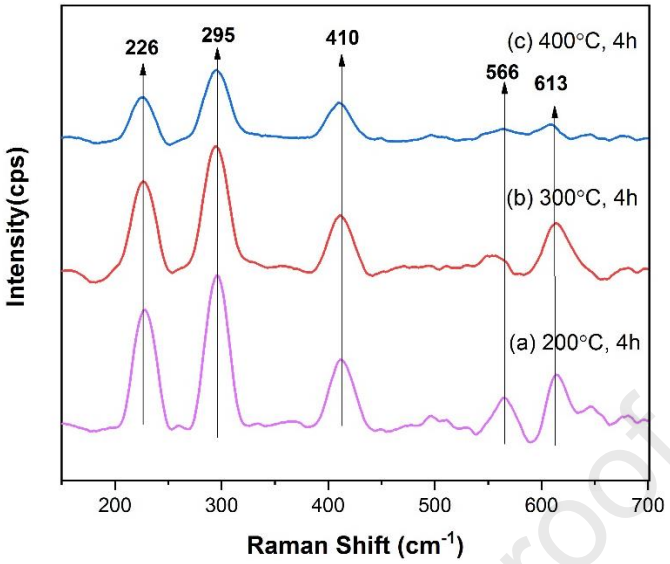

Fig. 7. Raman Spectra of the hematite nanoparticles calcined at different temperature.

3.5 TEM and EDS analysis

The TEM image with EDS analysis of α-Fe_2O_3 nanoparticles calcined at 300°C, 4hours are depicted in Fig. 8. The surface morphology of the nanoparticles are mostly agglomerated in nature which are the common tendency of nanoparticles. The average particle size is 13.49 nm. The purity of the nanomaterials were also examined by EDS analysis with the existence of elemental confirmation which indicate that synthesized hematite nano materials are composed of Fe and O. This data is in good agreement with the data obtained from SEM-EDS. The high resolution TEM (HRTEM) gives the crystal lattice fringe spacing between the crystal lattice plane (104) and the calculated value is 0.270 nm. HRTEM also shows uniform lattice crystal structure without detectable defects [45]. The selected area electron diffraction (SAED) pattern also shows the poly crystalline behavior of the hematite nanoparticles with cubic crystal structure.

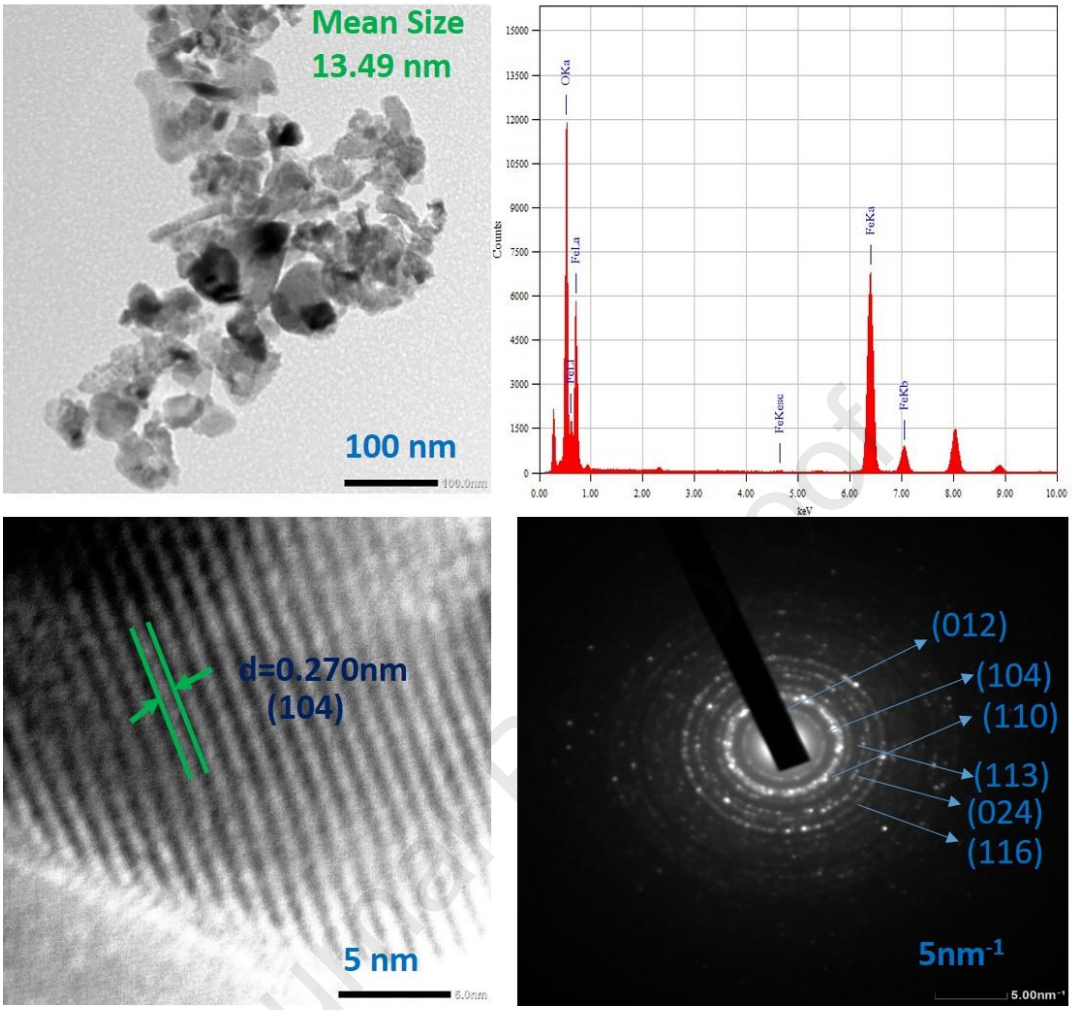

Fig. 8. TEM image with EDS data and selected area diffraction pattern of α-Fe_2O_3 nanoparticles calcined at 300°C, 4hours

3.6 Optical properties

The optical properties of the synthesized hematite nanoparticles measured at the wavelength range of 200-800nm have been shown in Fig. 9. By using Kubelka-Munk function, absorption data obtained from the reflectance was used to evaluate the optical nature of synthesized hematite nanoparticles. The spectrum shows four absorption band in the UV-visible region as shown in Fig. 9(b). The first absorbed region was found to be in the range of 300-400 nm and it has been centered at 347 nm which is basically due to the metal charge transfer transition between valence band and conduction band. The second absorption band was located at the wavelength region of 401.57 nm is attributed at ligand to field transition due to the contribution of Fe^{3+} ligand field transition. The maximum absorption band was recorded in the visible light region at 518 nm could be assigned as

pair excitation between neighboring Fe^{3+} - Fe^{3+} cation [5–7,51]. The other absorption band observed at 662.25 nm is responsible for ligand field transition. The optical band gap energy (E_g) of the synthesized α-Fe_2O_3 nanoparticles was estimated by using Kubelka-Munk function.

$$F(R) = \frac{(1-R)^2}{2R} = \frac{K}{S} \quad (10)$$

Where R is the absolute reflectance of the sample, K is the molar absorption coefficient and S is the scattering coefficient. The band energy gap was plotted as $(F(R)\ hv)^2$ vs hv which is shown in Fig. 9(c) . The increase of calcination temperature having low crystallite size and grain size have affected the low band gap energy value within the range of 2.30-2.42 eV as recorded in Table 2. Microstructural characteristic is greatly affected by the E_g value and it is influenced by various factors such as surface/ interface structure, grain size, crystal quality, lattice parameters, lattice strain, carrier concentrations, defect structure, and chemical composition [52]. Eg slighty shifts to 2.30 to 2.42 eV compared to that of pure α-Fe_2O_3 (2.1 eV) with decreasing calcination temperature. The decreasing is attributed to the size effect, as the crystallite size of the samples decreased with increasing the calcination temperature [26]. XRD measurements clearly indicate that single phase formation is commenced for 200°C with Eg value 2.42 and increasing calcination temperatures have significant effect on Eg values.

Table 2

Optical band gap energy of α-Fe_2O_3 nano particles calcined at different temperature

Sample	Band gap, E_g (eV)
200°C , 4h	2.42
300°C , 4h	2.37
400°C , 4h	2.30

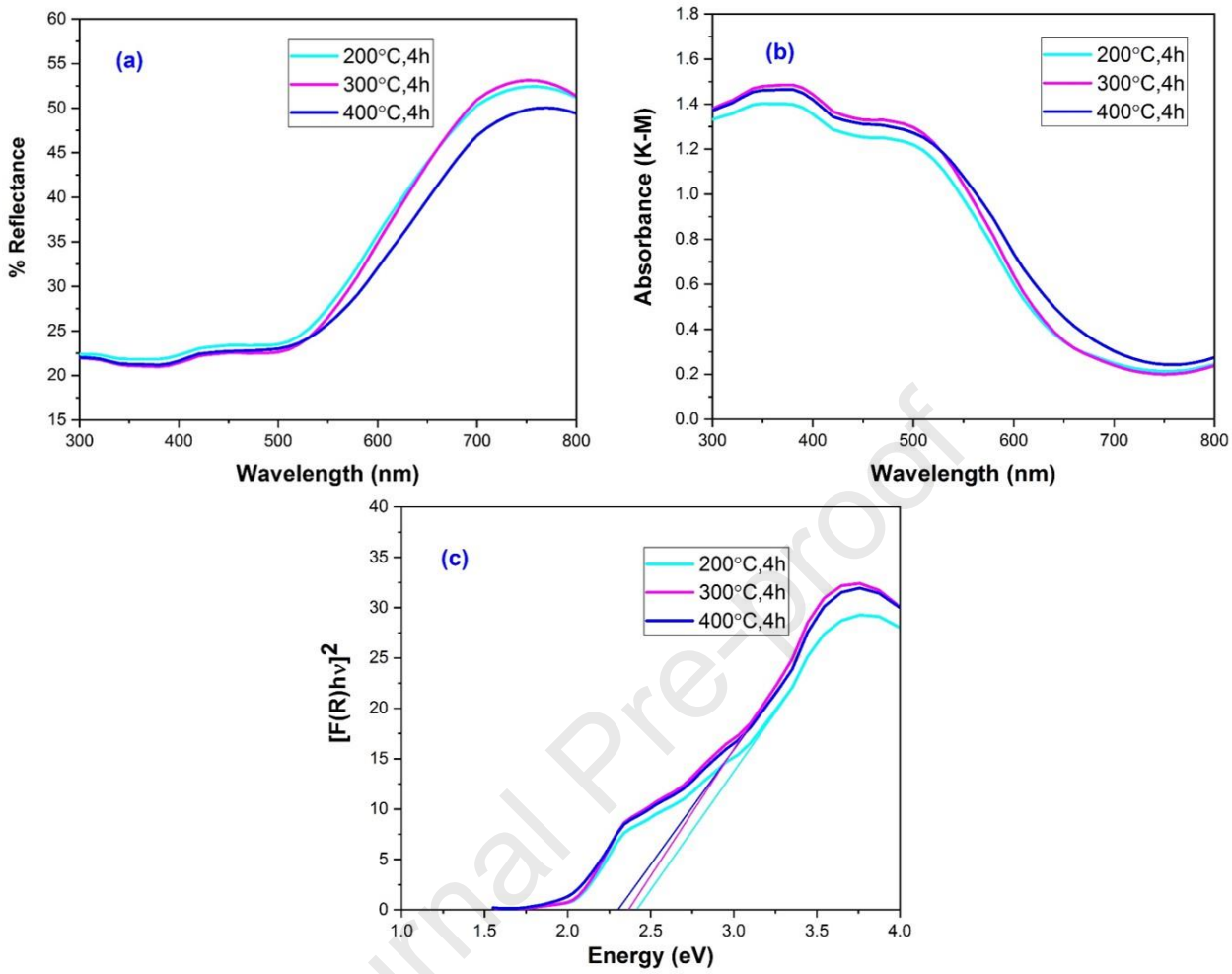

Fig. 9. The optical properties of hematite nanoparticles calcined at different temperature (a) UV-Vis diffuse reflectance spectra (b) UV-Vis absorbance spectra (c) Band gap energy

3.7 Particle size analysis by DLS

Particle size distribution of hematite nanoparticles measured by dynamic light scattering method (DLS) are shown in Fig. 10. The hydrodynamic diameter $\overline{D}_h$ was calculated from the Z-average translation diffusion coefficient $\overline{D}$ through the Stokes-Einstein Eq. [53]:

$$\overline{D}_h = \frac{k_B T}{3\pi\eta\overline{D}} \qquad (11)$$

Where k_B is the Boltzmann constant and $\eta$is the solvent viscosity at temperature T. The Z-average apparent hydrodynamic diameter $\overline{D}_h$ and polydispersity index (PDI) are recorded in Table 3. It is clearly seen from the table that the Z-average and the PDI values of all the hematite nanoparticles are nearly same which also indicates the poly dispersity of the particles. The mean particle size

determined by dynamic light scattering (DLS) is larger than the crystallite size calculated from X-ray diffraction (XRD) data. This discrepancy arises because DLS measures the hydrodynamic diameter, reflecting the time-dependent fluctuations in scattered light intensity caused by the Brownian motion of the particles. Consequently, higher hydrodynamic particle size values suggest that the nanoparticles tend to agglomerate, forming larger clusters when dispersed in a solvent [33]. Agglomeration or aggregation often renders nanoparticles less stable, resulting in a more heterogeneous mixture that can lead to inconsistent properties and performance. In contrast, homogeneous particles tend to exhibit greater stability [54]. The PDI values and the average particles size of the hematite nanoparticles indicate that the synthesized samples are notably polydisperse. There is no significant change in particle sizes with increasing temperature.

Table 3

Z-average hydrodynamic diameter $\overline{D}_h$ and polydispersity index (PDI) of α-Fe_2O_3 nanoparticles calcined at low temperature and time

Sample	$\overline{D}_h$nm	PDI
200°C, 4h	220	0.3532
300°C, 4h	226	0.3953
400°C, 4h	224	0.3534

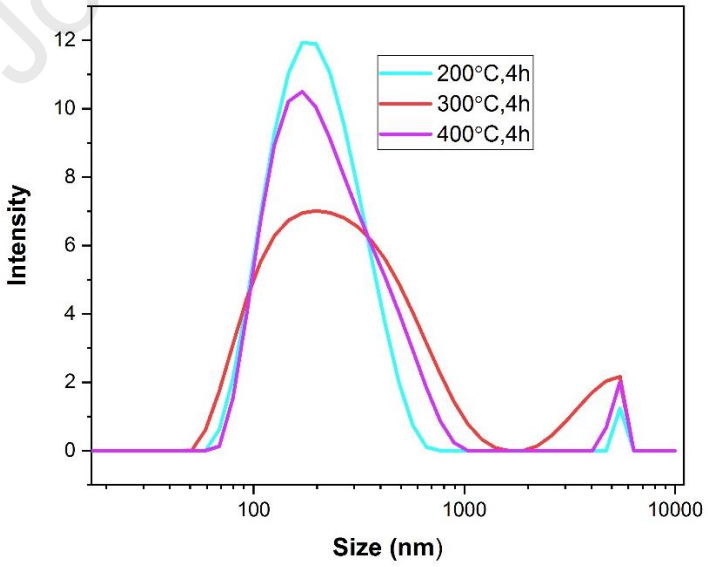

Fig. 10. Particle size distribution of α-Fe_2O_3 nanoparticles calcined at different temperature

3.8 Chemical state analysis by XPS

X-ray photoelectron spectroscopy (XPS) is the suitable technique for identifying precisely the oxidation state of Fe and O atoms of hematite nanoparticles. The survey spectrum and the high resolution XPS spectra of Fe 2p calcined at 300°C, 4h are shown in Fig. 11. The nanoparticles were primarily composed of Fe and O atoms. The peak position corresponding to Fe 2p has been searched in the binding energy range 705-730. The peaks position having binding energy 710.93 eV and 724.33 eV representing the Fe^{3+}2p 3/2 and Fe^{3+}2p 1/2 with a satellite peak observed at 718.95 eV also indicate the Fe^{3+}2p 3/2 agreeing very closely the previously reported [8,44,55–58]. Hematite and maghemite exhibit nearly identical spectra. However, the difference in lattice structure (cubic vs .hexagonal) does not impact on chemical shift. In survey spectrum C 1s peak observed at 284.8 eV is responsible for adventitious carbon contamination. Therefore, the XPS studies indicate iron in Fe^{3+} which confirm the formation of Fe_2O_3 as well as the crystal phase α-Fe_2O_3 has already identified by XRD.

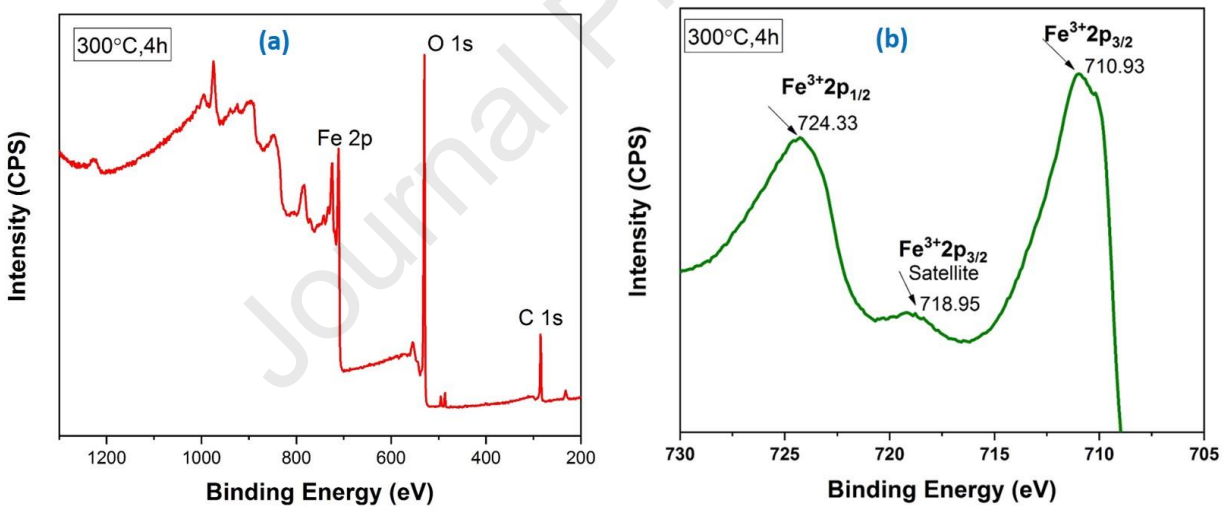

Fig. 11. XPS data of α-Fe_2O_3 nanoparticles (a) survey spectrum data calcined at 300°C, 4 h (b) Fe 2p spectrum calcined at 300°C, 4 h

4. Comparative study

A detailed comparison of hematite nanoparticles synthesized by different methods is presented in Table 4, highlighting the variations in synthesis conditions.

Table 4

Comparison of current research with the literature

Sample	Synthesis procedure	Temperature (°C)	Time (h)	Ref.
α-Fe_2O_3	Green and Chemical method	200, 300 and 500	2,4 and 5	[59]
α-Fe_2O_3	Hydrothermal method	160 and 180	10 and 12	[60]
α-Fe_2O_3	Green synthesis	60	-	[61]
α-Fe_2O_3/Fe_3O_4	Combustion-Calcination	200, 250 ,300, 350 and 400	2	[32]
α-Fe_2O_3	Calcination	800 and 900	1	[62]
α-Fe_2O_3	Oxidation-Calcination	200, 300 and 400	4	Present work

5. Conclusion

Hematite (α-Fe_2O_3) nanoparticles have been successfully synthesized from waste condensed milk containers and the effect of low temperature calcination on the synthesized samples have also been studied. Structural, morphological and optical nature of the α-Fe_2O_3 nanoparticles were investigated by different characterization techniques. Hematite phase can be successfully prepared at 200°C, as confirmed by various structural analyses. Crystallite size measurements indicate that, with increasing calcination temperature, the crystallite size decreases, ranging from 13.07 to 34.57 nm across different methods. The morphological analysis and elemental composition of the synthesized α-Fe_2O_3 nanoparticles reveal noticeable agglomeration behavior, confirming that the nanoparticles are composed solely of iron (Fe) and oxygen (O). The XPS data also provides the surface chemistry and oxidation state of Fe 2p and O1s which also supported the purity of the hematite nanoparticles calcined at 300°C, 4h. Optical properties and band gap analysis measured from Kubelka-Munk function exhibit that the optical band gap energy slightly decreases with increasing temperature which can be used as a photo catalytic dye degradation. The mean particle size are quite similar for distinct calcination temperature 200, 300 and 400°C with the values of 220, 226 and 224 nm respectively. In conclusion, the hematite (α-Fe_2O_3) nanoparticles synthesized

from waste condensed milk container show great potential as a versatile material for various application such as photo catalyst, pigment, sensors etc.

Data availability statement

Data will be made available on request from authors.

Declaration of competing interest

The authors declare that they have no known competing financial interests or personal relationships that could have appeared to influence the work reported in this paper.

Declaration of generative AI

No AI software was used to prepare the manuscript.

Acknowledgement

The authors are grateful for the financial support from Bangladesh Council of Scientific and Industrial Research (BCSIR). The authors would like to thank Institute of Glass and Ceramic Research and Testing (IGCRT), Institute of Energy Research and Development (IERD), Central Analytical Research and Facilities (CARF), BCSIR for providing technical supports.

References

[1] E. Esmaeili, M. Salavati-Niasari, F. Mohandes, F. Davar, H. Seyghalkar, Modified single-phase hematite nanoparticles via a facile approach for large-scale synthesis, Chem. Eng. J. 170 (2011) 278–285. https://doi.org/10.1016/j.cej.2011.03.010.

[2] S.C.K.G.. S.B.A.H. Bagheri, Generation of Hematite Nanoparticles via Sol-Gel Method, Res. J. Chem. Sci. 3 (2013) 62–68. http://www.isca.in/rjcs/Archives/vol3/i7/9.ISCA-RJCS-2013-097.pdf.

[3] S. Sagadevan, R.P. Sivasankaran, J.A. Lett, I. Fatimah, SS symmetry Evaluation of Photocatalytic Activity and Electrochemical Properties of Hematite Nanoparticles, (2023).

[4] K. Omri, I. Najeh, L. El Mir, Author ' s Accepted Manuscript, Ceram. Int. (2016). https://doi.org/10.1016/j.ceramint.2016.02.151.

[5] E. Paulson, M. Jothibas, Significance of thermal interfacing in hematite (α -Fe 2 O 3) nanoparticles synthesized by sol-gel method and its characteristics properties, Surfaces and Interfaces. 26 (2021) 101432. https://doi.org/10.1016/j.surfin.2021.101432.

[6] O. Nanoparticles, L.E. Mathevula, L.L. Noto, B.M. Mothudi, M.S. Dhlamini, Author ' s Accepted Manuscript Structural and Optical properties of sol-gel derived, J. Lumin. (2017). https://doi.org/10.1016/j.jlumin.2017.07.055.

[7] A. Rufus, N. Sreeju, D. Philip, RSC Advances applications, RSC Adv. 6 (2016) 94206–94217. https://doi.org/10.1039/C6RA20240C.
[8] J. Khanam, R. Hasan, B. Biswas, S. Akter, N. Sharmin, S. Ahmed, S. Al-reza, Heliyon Development of ceramic grade red iron oxide pigment from waste iron source, 9 (2023).
[9] M.M.K. Omri, M.E.S.G.F. Alharbi, Elaboration and influence of annealing process on physico - chemical properties of silica – titania nanocomposites, Appl. Phys. A. 127 (2021) 1–8. https://doi.org/10.1007/s00339-021-04593-8.
[10] S. Mizuno, H. Yao, Journal of Magnetism and Magnetic Materials On the electronic transitions of α-Fe 2 O 3 hematite nanoparticles with different size and morphology : Analysis by simultaneous deconvolution of UV – vis absorption and MCD spectra, J. Magn. Magn. Mater. 517 (2021) 167389. https://doi.org/10.1016/j.jmmm.2020.167389.
[11] B. Gilbert, C. Frandsen, E.R. Maxey, D.M. Sherman, Band-gap measurements of bulk and nanoscale hematite by soft x-ray spectroscopy, (2009). https://doi.org/10.1103/PhysRevB.79.035108.
[12] J.S. Justus, S.D.D. Roy, A.M.E. Raj, Synthesis and characterization of hematite nanopowders, Mater. Res. Express. 3 (n.d.) 1–9. https://doi.org/10.1088/2053-1591/3/10/105037.
[13] L. Han, H. Liu, Y. Wei, In situ synthesis of hematite nanoparticles using a low-temperature microemulsion method, Powder Technol. 207 (2011) 42–46. https://doi.org/10.1016/j.powtec.2010.10.008.
[14] D.A. Maz´on-Montijo, D. Cabrera-German, A.S. S´anchez-Ovando, O. Y. Ramírez-Esquivel, Z. Montiel-Gonz´alez, Role of morphology , composition , and structure on the optical response of nanostructured hematite thin films, Optical Materials. 110 (2020).
[15] M. Science-poland, Influence of different materials on the microstructure and optical band gap of α -Fe 2 O 3 nanoparticles, 32 (2014) 193–197. https://doi.org/10.2478/s13536-013-0171-z.
[16] C. Lohaus, C. Steinert, J. Brötz, A. Klein, Systematic Investigation of the Electronic Structure of Hematite Thin Films, 1700542 (2017) 1–8. https://doi.org/10.1002/admi.201700542.
[17] N. Popov, M. Risti, M. Bo, D. Stankovi, S. Krehula, Influence of Sn doping on the structural , magnetic , optical and photocatalytic properties of hematite (α -Fe 2 O 3) nanoparticles, 161 (2022). https://doi.org/10.1016/j.jpcs.2021.110372.
[18] K. de Fátima Ulbrich, C.E.M. de Campos, Obtaining of hematite from industrial steel waste using dry-milling and high temperature, Clean. Eng. Technol. 5 (2021). https://doi.org/10.1016/j.clet.2021.100327.
[19] B. Liu, S. Zhang, D. Pan, C. Chang, Synthesis and Characterization of Micaceous Iron Oxide Pigment from Oily Cold Rolling Mill Sludge, Procedia Environ. Sci. 31 (2016) 653–661. https://doi.org/10.1016/j.proenv.2016.02.121.
[20] E. Darezereshki, One-step synthesis of hematite (α-Fe2O3) nano-particles by direct thermal-decomposition of maghemite, Mater. Lett. 65 (2011) 642–645. https://doi.org/10.1016/j.matlet.2010.11.030.
[21] D.M.S.N. Dissanayake, M.M.M.G.P.G. Mantilaka, T.C. Palihawadana, G.T.D. Chandrakumara, R.T. De Silva, H.M.T.G.A. Pitawala, K.M. Nalin De Silva, G.A.J. Amaratunga, Facile and low-cost synthesis of pure hematite (α-Fe2O3) nanoparticles from naturally occurring laterites and their superior adsorption capability towards acid-dyes, RSC Adv. 9 (2019) 21249–21257. https://doi.org/10.1039/c9ra03756j.

[22] L.M. Khoiroh, M.N. Al-Chabib, A. Prasetyo, Synthesis and characterization of hematite (α-Fe2O3) from lathe waste using co-precipitation -calcination method, IOP Conf. Ser. Mater. Sci. Eng. 578 (2019). https://doi.org/10.1088/1757-899X/578/1/012004.

[23] H. Mansour, H. Letifi, R. Bargougui, S. De Almeida, D. Beatrice, Structural , optical , magnetic and electrical properties of hematite (α-Fe 2 O 3) nanoparticles synthesized by two methods : polyol and precipitation, Appl. Phys. A. 0 (2017) 0. https://doi.org/10.1007/s00339-017-1408-1.

[24] H.M. Asoufi, T.M. Al-Antary, A.M. Awwad, Green route for synthesis hematite (α-Fe2O3) nanoparticles: Toxicity effect on the green peach aphid, Myzus persicae (Sulzer), Environ. Nanotechnology, Monit. Manag. 9 (2018) 107–111. https://doi.org/10.1016/j.enmm.2018.01.004.

[25] D. Hassan, A.T. Khalil, J. Saleem, A. Diallo, S. Khamlich, Z.K. Shinwari, M. Maaza, Biosynthesis of pure hematite phase magnetic iron oxide nanoparticles using floral extracts of Callistemon viminalis (bottlebrush): their physical properties and novel biological applications, Artif. Cells, Nanomedicine Biotechnol. 46 (2018) 693–707. https://doi.org/10.1080/21691401.2018.1434534.

[26] R. Al-gaashani, S. Radiman, N. Tabet, A.R. Daud, Rapid synthesis and optical properties of hematite (a -Fe 2 O 3) nanostructures using a simple thermal decomposition method, J. Alloys Compd. 550 (2013) 395–401. https://doi.org/10.1016/j.jallcom.2012.10.150.

[27] X. Cui, T. Liu, Z. Zhang, L. Wang, S. Zuo, W. Zhu, Hematite nanorods with tunable porous structure : Facile hydrothermal-calcination route synthesis , optical and photocatalytic properties, Powder Technol. 266 (2014) 113–119. https://doi.org/10.1016/j.powtec.2014.06.028.

[28] T. Nurhayati, F. Iskandar, M. Abdullah, Syntheses of Hematite (□ -Fe 2 O 3) Nanoparticles Using Microwave-Assisted Calcination Method, (2013). https://doi.org/10.4028/www.scientific.net/MSF.737.197.

[29] A. Biswas, A.K. Patra, S. Sarkar, D. Das, D. Chattopadhyay, S. De, Synthesis of highly magnetic iron oxide nanomaterials from waste iron by one-step approach, Colloids Surfaces A. 589 (2020) 124420. https://doi.org/10.1016/j.colsurfa.2020.124420.

[30] E. Metin, A. Ero, Solid waste management practices and review of recovery and recycling operations in Turkey, 23 (2003) 425–432. https://doi.org/10.1016/S0956-053X(03)00070-9.

[31] D. Anghinolfi, M. Paolucci, M. Robba, A. Celeste, A dynamic optimization model for solid waste recycling, 33 (2013) 287–296.

[32] T. Liu, S. Zhang, Z. Wang, Y. Xu, Preparation and characterization of α-Fe2O3/Fe3O4heteroplasmon nanoparticles via the hydrolysis-combustion-calcination process of iron nitrate, Mater. Res. Express. 9 (2022). https://doi.org/10.1088/2053-1591/ac68c6.

[33] S.S.Æ.S. Lee, Æ.J. Wook, P.S.S. Prasad, Æ.K.J.Æ.Y. Shul, Effect of Calcination Temperature on the Activity and Cobalt Crystallite Size of Fischer – Tropsch Co – Ru – Zr / SiO 2 Catalyst, (2009) 233–239. https://doi.org/10.1007/s10562-008-9803-z.

[34] N. Méndez-lozano, L.M. Apátiga-castro, E.M. Rivera-muñoz, A. Manzano-ramirez, C.A. Gonzalez-gutierrez, M.A. Zamora-antuñano, V. De México, C. Querétaro, B. Juriquilla, A. Del, S. Rosa, Crystal growth of hydroxyapatite microplates synthesised by Sol – Gel method, 14 (2019) 1414–1417. https://doi.org/10.1049/mnl.2019.0402.

[35] H. Mansour, K. Omri, S. Ammar, Structural, optical and magnetic properties of cobalt

doped hematite nanoparticles, Chem. Phys. 525 (2019) 110400. https://doi.org/10.1016/j.chemphys.2019.110400.
[36] H. Sarma, K.C. Sarma, X-ray Peak Broadening Analysis of ZnO Nanoparticles Derived by Precipitation method, 4 (2014) 1–7.
[37] V. S. S. Kumar, K. V. Rao., X-ray Peak Broadening Analysis and Optical Studies of ZnO Nanoparticles Derived by Surfactant Assisted Combustion Synthesis, Journal of Nano- and Electronic Physics. Vol. 5 No 2, 02026(6pp) (2013)1–6.
[38] D. Nath, F. Singh, R. Das, X-ray diffraction analysis by Williamson-Hall, Halder-Wagner and size-strain plot methods of CdSe nanoparticles- a comparative study, Mater. Chem. Phys. 239 (2020) 122021. https://doi.org/10.1016/j.matchemphys.2019.122021.
[39] H. Bantikatla, L.D.N.S.M. P, R. Kanth, Materials Today : Proceedings Microstructural parameters from X-ray peak profile analysis by Williamson-Hall models ; A review, Mater. Today Proc. (2021) 6–11. https://doi.org/10.1016/j.matpr.2021.06.256.
[40] S.S. Jahil, I.A. Mohammed, A.R. Khazaal, K.A. Jasim, K.H. Harbbi, Application the Halder – Wagner to Calculation Crystal Size and Micro Strain by X-ray Diffraction Peaks Analysis, (2022). https://doi.org/10.14704/nq.2022.20.1.NQ22074.
[41] S.K. Sen, U.C. Barman, M.S. Manir, P. Mondal, X-ray peak pro fi le analysis of pure and Dy-doped α -MoO 3 nanobelts using Halder-Wagner methods, (2020).
[42] D.E. Fouad, C. Zhang, H. El-Didamony, L. Yingnan, T.D. Mekuria, A.H. Shah, Improved size, morphology and crystallinity of hematite (α-Fe2O3) nanoparticles synthesized via the precipitation route using ferric sulfate precursor, Results Phys. 12 (2019) 1253–1261. https://doi.org/10.1016/j.rinp.2019.01.005.
[43] M. Tahir, M. Fakhar-e-alam, M. Atif, G. Mustafa, Z. Ali, Journal of King Saud University – Science Investigation of optical , electrical and magnetic properties of hematite a -Fe 2 O 3 nanoparticles via sol-gel and co-precipitation method, J. King Saud Univ. - Sci. 35 (2023) 102695. https://doi.org/10.1016/j.jksus.2023.102695.
[44] M. Zhu, Y. Wang, D. Meng, X. Qin, G. Diao, Hydrothermal synthesis of hematite nanoparticles and their electrochemical properties, J. Phys. Chem. C. 116 (2012) 16276–16285. https://doi.org/10.1021/jp304041m.
[45] Y. Xu, S. Yang, G. Zhang, Y. Sun, D. Gao, Y. Sun, Uniform hematite α-Fe2O3 nanoparticles: Morphology, size-controlled hydrothermal synthesis and formation mechanism, Mater. Lett. 65 (2011) 1911–1914. https://doi.org/10.1016/j.matlet.2011.03.085.
[46] T. Gong, Y. Tang, Preparation of multifunctional nanocomposites Fe3O4@SiO2-EDTA and its adsorption of heavy metal ions in water solution, Water Sci. Technol. 81 (2020) 170–177. https://doi.org/10.2166/wst.2020.099.
[47] I. V Chernyshova, M.F. Hochella, P. Northwest, A.E. Madden, Size-dependent structural transformations of hematite nanoparticles . 1 . Phase transition w z, (2007). https://doi.org/10.1039/b618790k.
[48] Y. Liu, R.D.L. Smith, Differentiating Defects and Their Influence on Hematite Photoanodes Using X-ray Absorption Spectroscopy and Raman Microscopy., ACS Appl. Mater, Interfaces. 14 (2022) 6615–6624.
[49] M. Khalil, J. Yu, N. Liu, R.L. Lee, hematite nanoparticles Hydrothermal synthesis , characterization , and growth mechanism of hematite nanoparticles, (2014). https://doi.org/10.1007/s11051-014-2362-x.
[50] J. Howe, D. Peddis, Structure and Morphology Evolution of Hematite (α -Fe 2 O 3) Nanoparticles in Forced Hydrolysis of Ferric Chloride, (n.d.) 2–8.

[51] W.R.W. Ahmad, M.H. Mamat, A.S. Zoolfakar, Z. Khusaimi, The Effect of Ultrasonic Irradiation to Hematite Nanorod Arrays Properties for Humidity Sensor Applications, (2023). https://doi.org/10.1109/CSPA57446.2023.10087704.
[52] R.S.C. Advances, O. Dy, K.K. Bharathi, M. Noor-a-alam, R.S. Vemuri, C. V Ramana, RSC Advances Correlation between microstructure , electrical and optical properties of, (2012) 941–948. https://doi.org/10.1039/c1ra00161b.
[53] C. Colombo, G. Palumbo, A. Ceglie, R. Angelico, Characterization of synthetic hematite (α-Fe 2O 3) nanoparticles using a multi-technique approach, J. Colloid Interface Sci. 374 (2012) 118–126. https://doi.org/10.1016/j.jcis.2012.02.003.
[54] H.T. Phan, A.J. Haes, What Does Nanoparticle Stability Mean?, 2019. https://doi.org/10.1021/acs.jpcc.9b00913.
[55] X. Huang, Y. Chen, E. Walter, M. Zong, Y. Wang, X. Zhang, O. Qafoku, Z. Wang, K.M. Rosso, Xiaopeng Huang, * Ying Chen, Eric Walter, Meirong Zong, Yang Wang, Xin Zhang, Odeta Qafoku, Zheming Wang, and Kevin M. Rosso *, (2019). https://doi.org/10.1021/acs.est.9b02946.
[56] M. Fondell, M. Gorgoi, M. Boman, A. Lindblad, Surface modification of iron oxides by ion bombardment – Comparing depth profiling by HAXPES and Ar ion sputtering, J. Electron Spectros. Relat. Phenomena. 224 (2018) 23–26. https://doi.org/10.1016/j.elspec.2017.09.008.
[57] A. Shchukarev, J.F. Boily, XPS study of the hematite-aqueous solution interface, Surf. Interface Anal. 40 (2008) 349–353. https://doi.org/10.1002/sia.2657.
[58] J.D. Desai, H.M. Pathan, S. Min, K. Jung, O.S. Joo, FT-IR , XPS and PEC characterization of spray deposited hematite thin films, 252 (2005) 1870–1875. https://doi.org/10.1016/j.apsusc.2005.03.135.
[59] J. Amin, A. Abdullah, M. Jim, A. Guerrero, Effect of Calcination Temperature and Time on the Synthesis of Iron Oxide Nanoparticles : Green vs . Chemical Method, (2023).
[60] M. Tadic, D. Trpkov, L. Kopanja, S. Vojnovic, M. Panjan, Hydrothermal synthesis of hematite (α-Fe2O3) nanoparticle forms: Synthesis conditions, structure, particle shape analysis, cytotoxicity and magnetic properties, J. Alloys Compd. 792 (2019) 599–609. https://doi.org/10.1016/J.JALLCOM.2019.03.414.
[61] M. Rizvi, T. Bhatia, R. Gupta, Green & sustainable synthetic route of obtaining iron oxide nanoparticles using Hylocereus undantus (pitaya or dragon fruit), Mater. Today Proc. 50 (2021) 1100–1106. https://doi.org/10.1016/j.matpr.2021.07.469.
[62] A. Ayuningtiyas, E.P. Hadisantoso, K. Wahyudi, Synthetize of Nano Particles a-Fe2O3 Material from Waste Magnetic Filter Ceramic Tile Industry Prepare by Calcination Method as Photocatalyst Degradation of Methylene Blue, J. Phys. Conf. Ser. 1912 (2021). https://doi.org/10.1088/1742-6596/1912/1/012020.

Declaration of interest

☒ The authors declare that they have no known competing financial interests or personal relationships that could have appeared to influence the work reported in this paper.

☐ The authors declare the following financial interests/personal relationships which may be considered as potential competing interests: